Supporting Information

Synergistic $WO_3 \cdot 2H_2O$ Nanoplates/WS_2 Hybrid Catalysts for High-Efficiency Hydrogen Evolution

Lun Yang[†], Xiaobin Zhu[†], Shijie Xiong[†], Xinglong Wu[†,*], Yun Shan[†,‡], and Paul K. Chu[§]

[†] *Key Laboratory of Modern Acoustics, MOE, Institute of Acoustics, Collaborative Innovation Center of Advanced Microstructures, National Laboratory of Solid State Microstructures, Nanjing University, Nanjing 210093, P. R. China*

[‡] *Key Laboratory of Advanced Functional Materials of Nanjing, Nanjing Xiaozhuang University, Nanjing 211171, P. R. China*

[§] *Department of Physics and Materials Science, City University of Hong Kong, Tat Chee Avenue, Kowloon, Hong Kong, China*

Corresponding Author

*hkxlwu@nju.edu.cn (XL Wu)

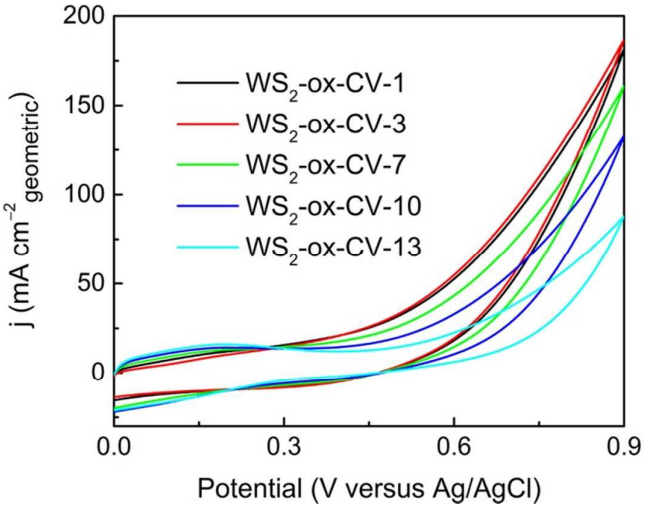

Figure S1. Cyclic voltammograms of the tungsten sulfide film prepared on CFP at 50 mV s^{-1} in 0.5 M H_2SO_4 for different cycle numbers.

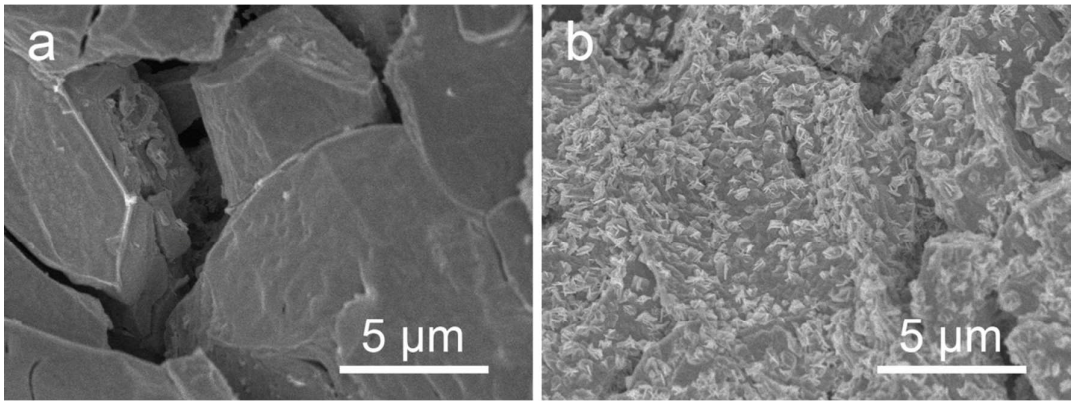

Figure S2. FE-SEM images of (a) WS_2−ox0 and (b) WS_2−ox6 on CFP.

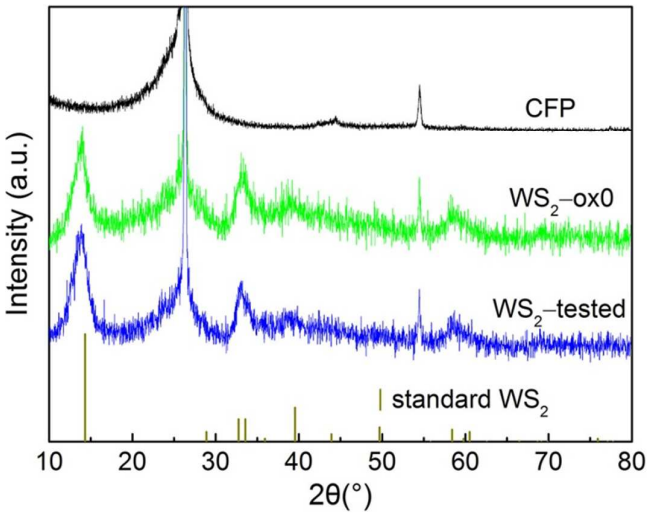

Figure S3. XRD patterns acquired from the CFP, WS_2–ox0 and WS_2–tested. The standard pattern of the 2H-WS_2 (JCPDS No.08-0237) is shown as reference.

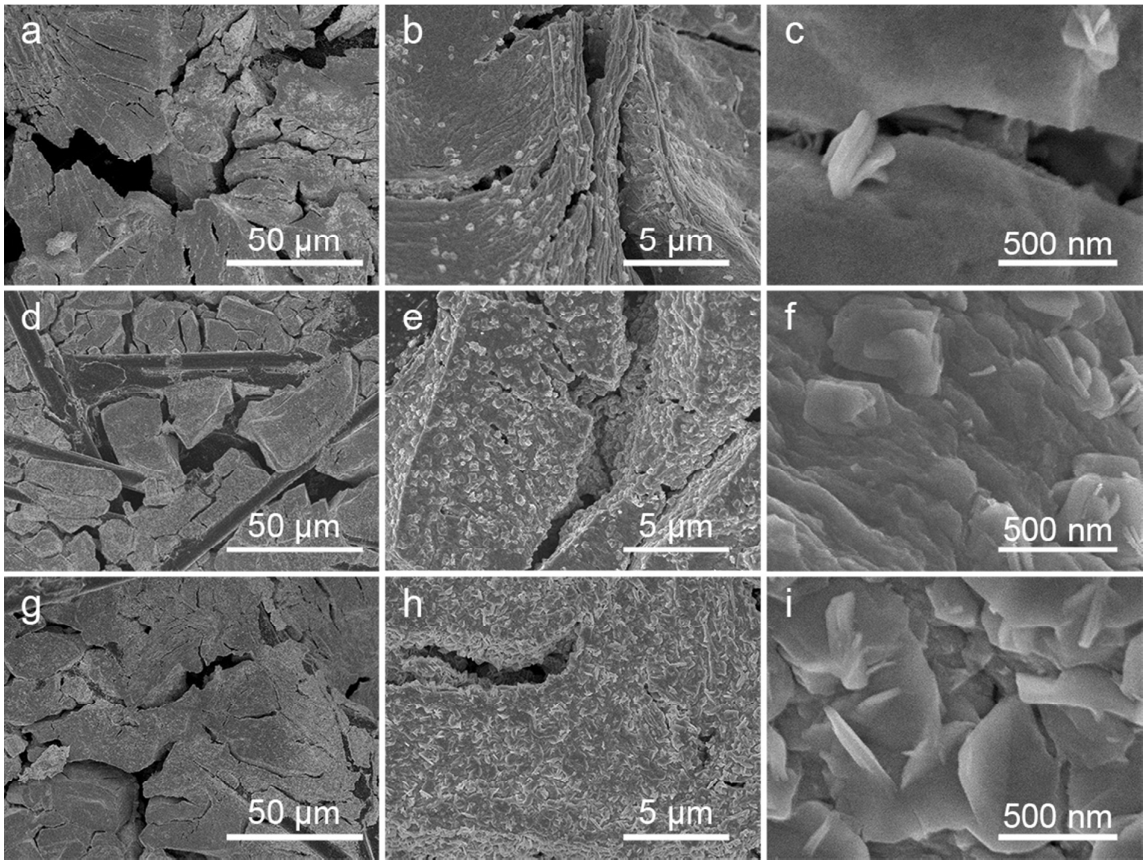

Figure S4. FE-SEM images of the catalyst films after different degree of anodization: (a, b, c) WS_2−ox2, (d, e, f) WS_2−ox4, and (g, h, i) WS_2−ox12.

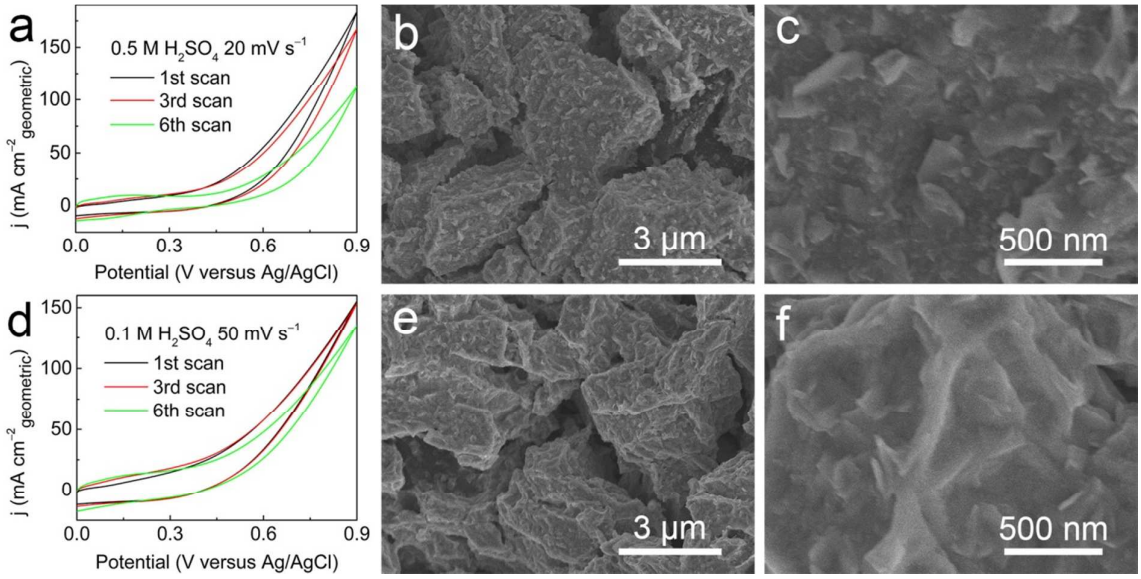

Figure S5. (a) Cyclic voltammograms of the tungsten sulfide film at 20 mV s^{-1} in 0.5 M H_2SO_4 for different cycle numbers. (b,c) FE-SEM images of the sample after anodization treatment in (a). (d) Cyclic voltammograms of the tungsten sulfide film at 50 mV s^{-1} in 0.1 M H_2SO_4 for different cycle numbers. (e,f) FE-SEM images of the sample after anodization treatment in (d).

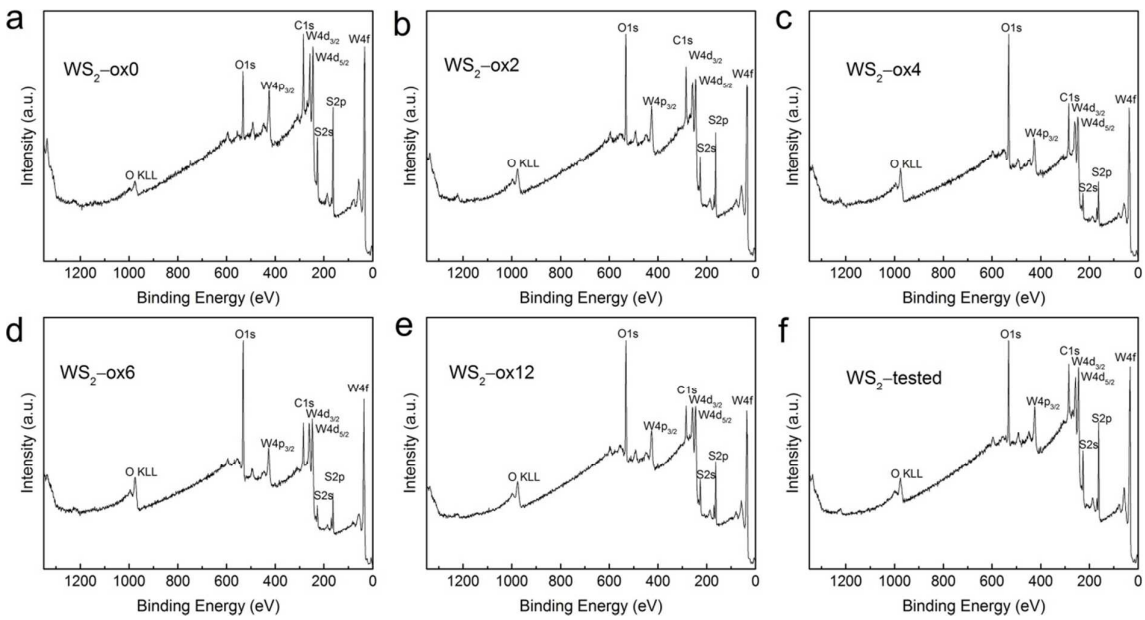

Figure S6. XPS survey spectra of the tungsten sulfide films after different anodization treatment (a-e) and the WS_2–tested sample (f).

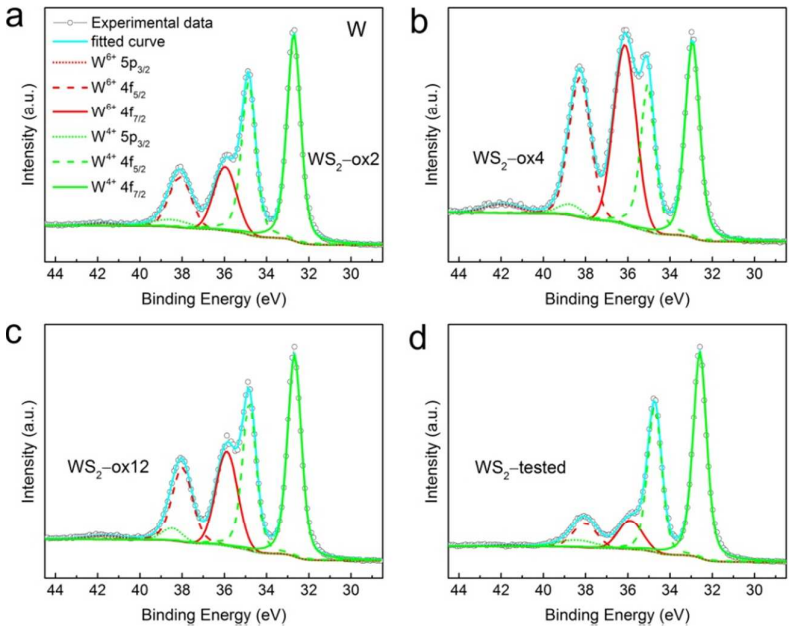

Figure S7. W *4f&5p* XPS spectra of (a) WS_2–ox2, (b) WS_2–ox4, (c) WS_2–ox12, and (d) WS_2–tested samples.

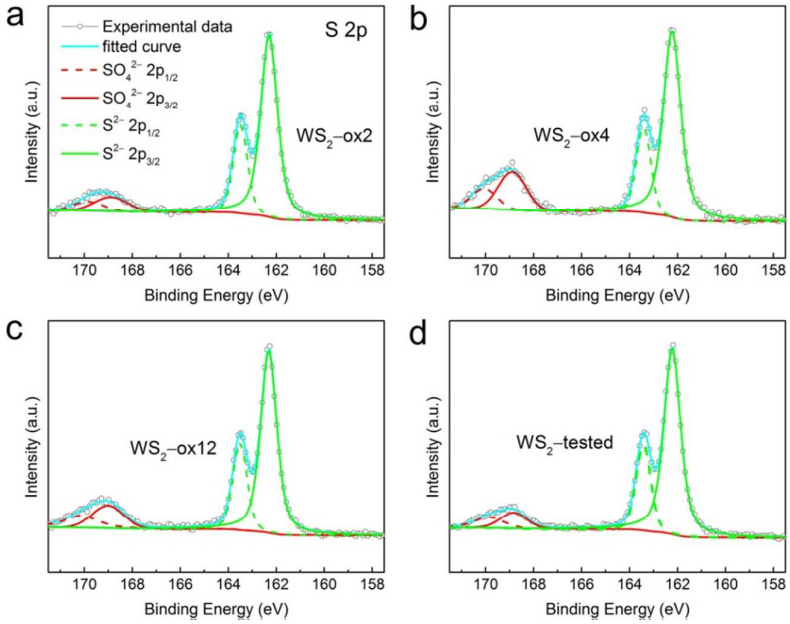

Figure S8. S *2p* XPS spectra of (a) WS_2–ox2, (b) WS_2–ox4, (c) WS_2–ox12, and (d) WS_2–tested samples.

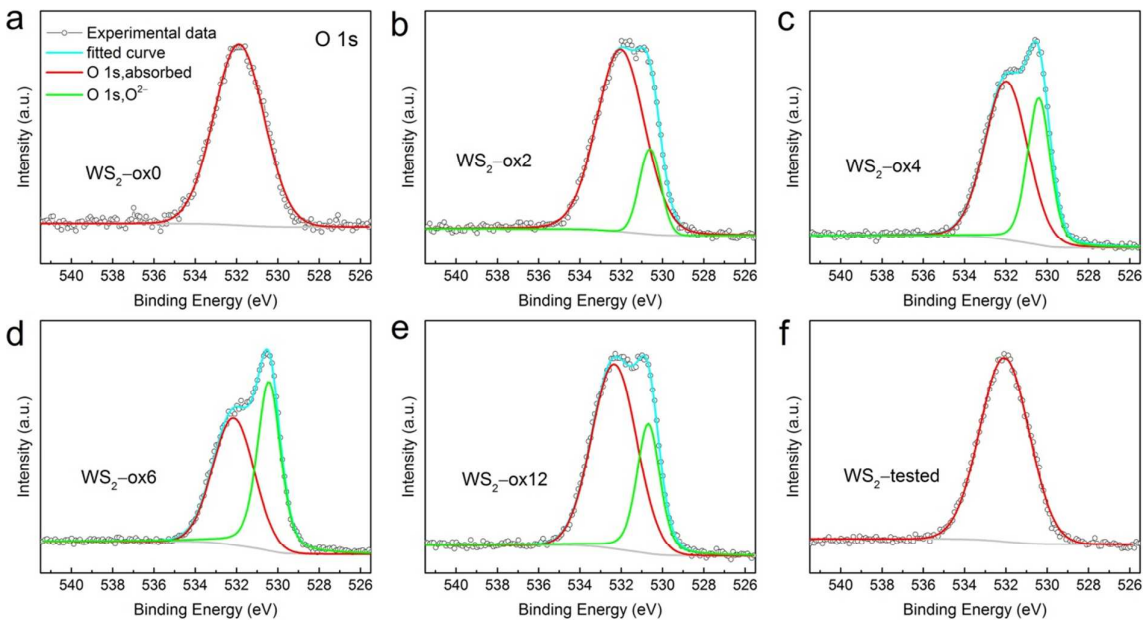

Figure S9. O *1s* XPS spectra of the tungsten sulfide films after different anodization treatment (a-e) and the WS_2–tested sample (f).

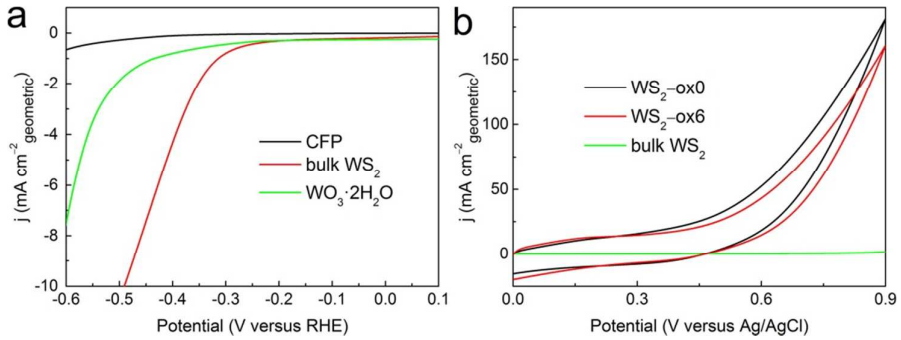

Figure S10. (a) Polarization curves of the CFP electrode, bulk WS_2 powder and pure $WO_3 \cdot 2H_2O$ particles in 0.5 M H_2SO_4 at a rate of 2 mV s^{-1} with iR correction. (b) Cyclic voltammetry results of WS_2–ox0, WS_2–ox6 and bulk WS_2 at a rate of 50 mV s^{-1}. The geometrical current density at 0.9 V vs. Ag/AgCl for WS_2–ox6 is 88.7% of the value of WS_2–ox0.

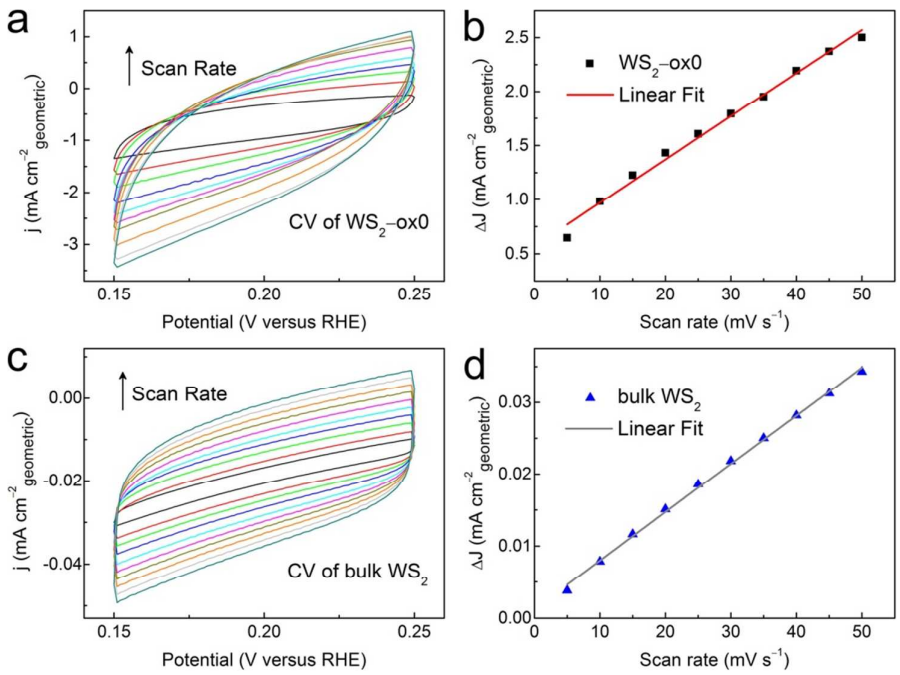

Figure S11. Cyclic voltammograms of (a) WS_2–ox0 and (c) bulk WS_2 measured at different scanning rates (5-50 mV s^{-1}) in 0.5 M H_2SO_4. Corresponding scanning rate dependence of ΔJ (the difference between anodic and cathodic geometrical current densities) at 0.20 V vs. RHE for (b) WS_2–ox0 and (d) bulk WS_2. The slope of the ΔJ versus scanning rate curve is twice the capacitance. The calculated double layer capacitance (C_{dl}) of WS_2–ox0 and bulk WS_2 powder are 20 and 0.34 mF cm^{-2}, respectively. Using the method presented in Refs. S1 and S2, the relative roughness factor (RF) of samples could be calculated by $RF = C_{dl}/C_{flat}$. C_{flat} is the capacitance for a flat electrode and is assumed to be 60 μF cm^{-2}.[S1,S2] So, the RF values for WS_2–ox0 and bulk WS_2 are 333.3 and 5.7, respectively. We suppose that the anodic current magnitude in Fig S10b is directly proportional to the amount of active sites in HER. Then the RF for WS_2–ox6 is obtained to be 295.7. The TOF values could be calculated by

$$\mathrm{TOF} = (\mathrm{j\ mA\ cm^{-2}})(1\ \mathrm{cm^2})\left(\frac{1}{2\times 1.602\times 10^{-19}\ \mathrm{C}}\right)\left(\frac{1}{\mathrm{RF}\times 1\ \mathrm{cm^2}/0.0876\ \mathrm{nm^2}}\right) = 2.73\times\frac{\mathrm{j}}{\mathrm{RF}}\ \mathrm{s^{-1}}$$.[S2,S3]

At a 150 mV overpotential, the geometrical current densities for WS_2–ox0 and WS_2–ox6 are 9.4 and 92.1 mA cm^{-2}, and their TOF values are 0.077 and 0.85 s^{-1}, respectively. The TOF performance of WS_2–ox6 is still inferior to that of 1T-WS_2 nanosheets,[S4] but it is better than amorphous MoS_x film with a TOF value of 0.8 s^{-1} at 220 mV overpotential.[S5]

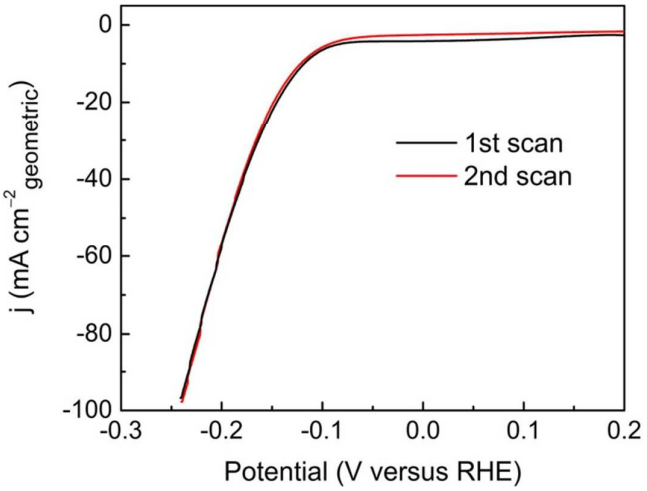

Figure S12. First (black line) and second (red line) polarization curves of WS_2–ox1 in 0.5 M H_2SO_4 at a scanning rate of 2 mV s^{-1}. Both curves have been corrected for the iR-loss.

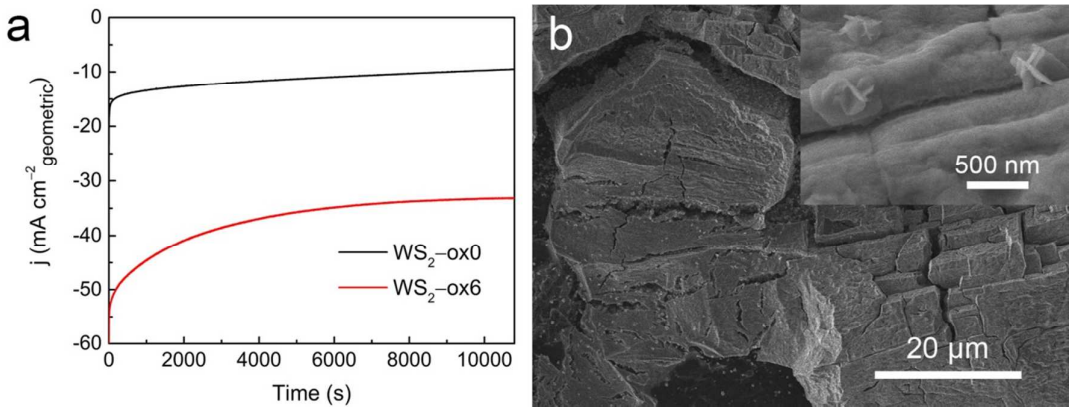

Figure S13. (a) Time dependence of the geometrical current density at –0.17 V vs. RHE without iR-correction in 0.5 M H_2SO_4 of WS_2–ox0 and WS_2–ox6. (b) FE-SEM images of the WS_2–ox6 sample after 3-h constant voltage electrolysis in (a). Compared to Figure 2b, the amount of $WO_3 \cdot 2H_2O$ nanoplates decreases obviously after the durability test.

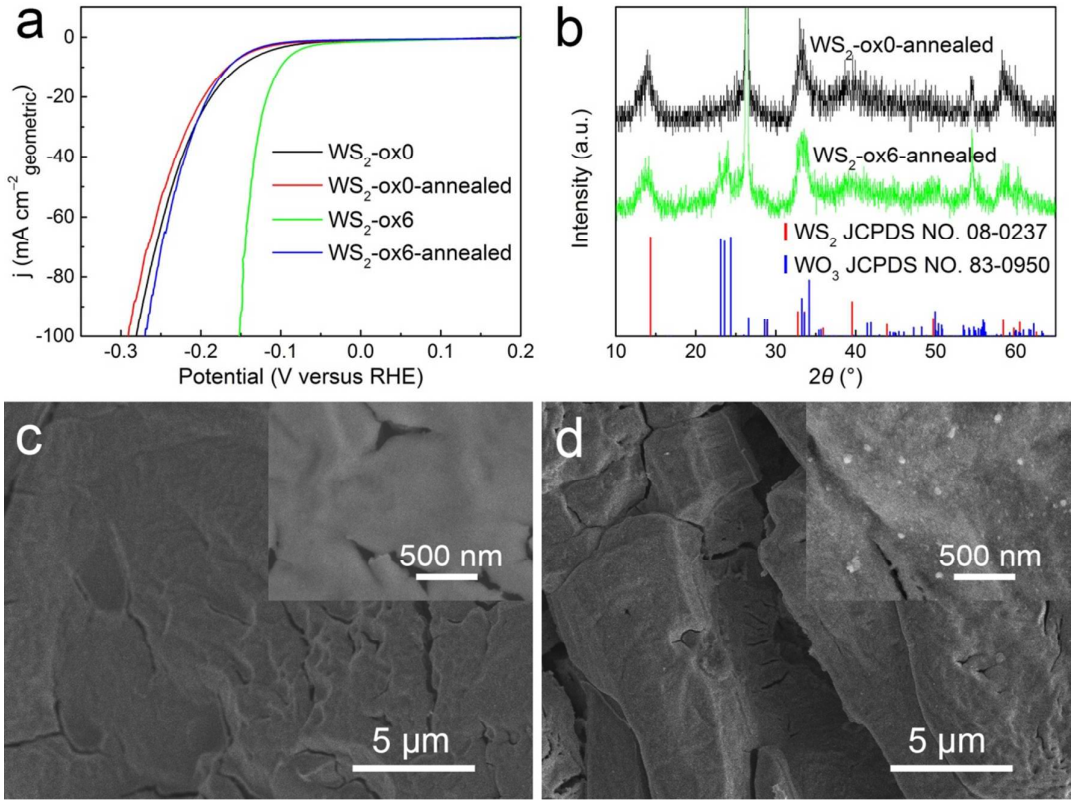

Figure S14. (a) Polarization curves obtained in 0.5 M H_2SO_4 at a rate of 2 mV s^{-1} with iR correction. WS_2–ox0–annealed and WS_2–ox6–annealed represent the WS_2–ox0 and WS_2–ox6 samples with the second annealing treatment under argon at 600 ^oC for 30 min, respectively. (b) XRD patterns of WS_2–ox0–annealed and WS_2–ox6–annealed. The standard patterns of the 2H-WS_2 (JCPDS No.08-0237) and monoclinic phase of WO_3 (JCPDS No.83-0950) are shown as reference. FE-SEM images acquired from samples of (c) WS_2–ox0–annealed and (d) WS_2–ox6–annealed. After the second heat treatment, the characteristic XRD peaks of the $WO_3 \cdot 2H_2O$ phase in WS_2–ox6 disappear, but new peaks corresponding to the WO_3 phase arise in the XRD patterns in (b). Moreover, irregular nanocrystals instead of nanoplates appear on the surface of WS_2–ox6–annealed in (d), which is supposed to have the WO_3 phase.

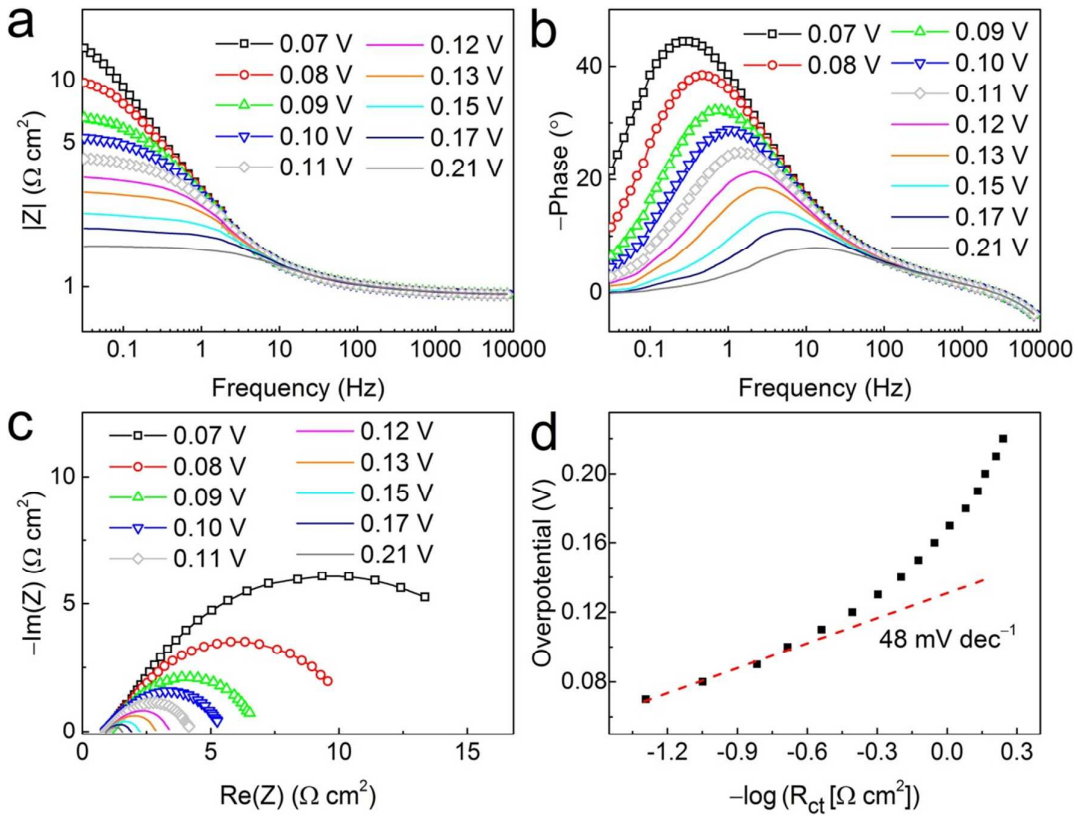

Figure S15. (a,b) Bode and (c) Nyquist plots of WS_2–ox6 obtained from the EIS measurements under various overpotentials in 0.5 M H_2SO_4. (d) Plots of overpotential versus $-\log R_{ct}$ for WS_2–ox6.

Table S1. Comparison of various HER catalysts in acid media. b is the Tafel slope and η stands for the overpotential.

Catalyst	Onset potential (mV)	b (mV dec^{-1})	η (mV) at 10 mA cm^{-2}	Ref
WS_2−ox6	~60	54	101	this work
$WO_3 \cdot 2H_2O$ particles	~300	148	620	
WO_3 nanoparticles	420	~122*	~569*	S6
WO_3 porous nanowires	~530*	56	598*	S7
WO_2-carbon mesoporous nanowires	35	46	58	
WO_3 powder	~519*	120	637	S8
$WO_{2.9}$ nanoparticles	~33*	50	70	
WS_2 nanoribbons	~150	68	225	S9
Ultrathin WS_2 nanoflakes	~100	48	~154*	S10
WS_2 quantum dots	~180	70	~336*	S11
WS_2 nanoparticles	~108*	68	~215*	S12
Amorphous NiWS	~100	55	265	S3
Amorphous CoWS	~120	74	330	
WS_2/Au hybrid	230	57	~367*	S13
WS_2@P, N, O-graphene film	~58*	52.7	125	S14
1T-WS_2 nanosheets	75	70	151	S15
$WS_{2(1-x)}Se_{2x}$ nanotubes (x = 0.52)	~173*	105	~267*	S16
Monolayer $WS_{2(1-x)}Se_{2x}$ (x = 0.43)	~34*	85	~59*	S17

(*) Calculated or read based on their data.

REFERENCES

(1) Tang, C. Y.; Wang, W.; Sun, A. K.; Qi, C. K.; Zhang, D. Z.; Wu, Z. Z.; Wang, D. Z. *ACS Catal.* **2015**, *5*, 6956-6963.

(2) Benck, J. D.; Chen, Z. B.; Kuritzky, L. Y.; Forman, A. J.; Jaramillo, T. F. ACS Catal. **2012**, *2*, 1916-1923.

(3) Yang, L.; Wu, X. L.; Zhu, X. S.; He, C. Y.; Meng, M.; Gan, Z. X.; Chu, P. K. *Appl. Surf. Sci.* **2015**, *341*, 149-156.

(4) Voiry, D.; Yamaguchi, H.; Li, J. W.; Silva, R.; Alves, D. C. B.; Fujita, T.; Chen, M. W.; Asefa, T.; Shenoy, V. B.; Eda, G.; Chhowalla, M. *Nat. Mater.* **2013**, *12*, 850-855.

(5) Merki, D.; Fierro, S.; Vrubel, H.; Hu, X. L. *Chem. Sci.* **2011**, *2*, 1262-1267.

(6) Ganesan, R.; Gedanken, A. *Nanotechnology* **2008**, *19*, 025702.

(7) Wu, R.; Zhang, J. F.; Shi, Y. M.; Liu, D. L.; Zhang, B. *J. Am. Chem. Soc.* **2015**, *137*, 6983-6986.

(8) Li, Y. H.; Liu, P. F.; Pan, L. F.; Wang, H. F.; Yang, Z. Z.; Zheng, L. R.; Hu, P.; Zhao, H. J.; Gu, L.; Yang, H. G. *Nat. Commun.* **2015**, *6*, 8064.

(9) Lin, J.; Peng, Z.W.; Wang, G.; Zakhidov, D.; Larios, E.; Yacaman, M. J.; Tour, J. M. *Adv. Energy Mater.* **2014**, *4*, 1301875.

(10) Cheng, L.; Huang, W. J.; Gong, Q. F.; Liu, C. H.; Liu, Z.; Li, Y. G.; Dai, H. J. *Angew. Chem. Int. Ed.* **2014**, *53*, 7860-7863.

(11) Xu, S. J.; Li, D.; Wu, P. Y. *Adv. Funct. Mater.* **2015**, *25*, 1127-1136.

(12) Chen, T. Y.; Chang, Y. H.; Hsu, C. L.; Wei, K. H.; Chiang, C. Y.; Li, L. J. *Int. J. Hydrogen Energy* **2013**, *38*, 12302-12309.

(13) Kim, J.; Byun, S.; Smith, A. J.; Yu, J.; Huang, J. X. *J. Phys. Chem. Lett.* **2013**, *4*, 1227-1232.

(14) Duan, J. J.; Chen, S.; Chambers, B. A.; Andersson, G. G.; Qiao, S. Z. *Adv. Mater.* **2015**, *27*, 4234-4241.

(15) Lukowski, M. A.; Daniel, A. S.; English, C. R.; Meng, F.; Forticaux, A.; Hamers, R. J.; Jin, S. *Energy Environ. Sci.* **2014**, *7*, 2608-2613.

(16) Xu, K.; Wang, F. M.; Wang, Z. X.; Zhan, X. Y.; Wang, Q. S.; Cheng, Z. Z.; Safdar, M.; He, J. *ACS Nano* **2014**, *8*, 8468-8476.

(17) Fu, Q.; Yang, L.; Wang, W. H.; Han, A.; Huang, J.; Du, P. W.; Fan, Z. Y.; Zhang, J. Y.; Xiang, B. *Adv. Mater.* **2015**, *27*, 4732-4738.